Identification of the material behavior of adhesive joints under dynamic multiaxial loadings

Anthony Janin, Andrei Constantinescu, Daniel Weisz-Patrault, Robert
Nevière, Matthieu Stackler, William Albouy

HAL Id: hal-02372694
https://hal.science/hal-02372694

Submitted on 20 Nov 2019

Identification of the material behavior of adhesive joints under dynamic multiaxial loadings

Anthony Janin[a], Andrei Constantinescu[a], Daniel Weisz-Patrault[a], Robert Neviere[b], Matthieu Stackler[b], William Albouy[b]

[a]LMS, École Polytechnique, CNRS, Université Paris-Saclay, 91128 Palaiseau, France
[b]Safran Composites, 33 avenue de la gare, 91760 Itteville, France

Abstract

This paper presents a numerical inverse method dedicated to the characterization of adhesive joints under multiaxial and dynamic loading conditions. The properties under scrutiny are the constitutive behavior of the joint as well as the final fracture surface. The experimental setup consists of a Split Hopkinson Pressure Bar system and local strain measurements performed by Digital Image Correlation (DIC) as well as a novel specific sandwich specimen denoted as DODECA. The direct numerical model is an original Finite Element computation combining 3D and 1D elements for an optimal handling of wave reflection and interfaces. It further provides an optimal compromise between computation time and accuracy. The identification method is based on the Finite Element Model Updating method (FEMU). Material parameters are identified for three different multiaxial loading conditions and presented as yield and fracture surfaces in the space of equivalent von Mises stress vs hydrostatic stress. As a complement of the analysis, uncertainties and confidence of the identified parameters are estimated with precise qualitative tools.

Keywords: Adhesive Joints, Behavior, Identification, Fracture, Inverse Method, Dynamic test

1. Introduction

The constraints of energy efficiency and weight reduction in structures and specifically in aeronautical applications have enforced the choice of adhesive joints as an interesting alternative to conventional methods such as riveting or screwing. However, the actual state of engineering for adhesive joints do not cover all aspects of material characterization to insure aircraft certification requirements for critical structural assemblies.

The difficulties of the material characterization of adhesive joints stem on the one hand side from the geometrical aspect ratio of joints and on the other hand side from the wide ranges of loading conditions. Joints can combine a thickness of several tens of microns with a span of several meters and are subject to quasi-static or dynamic multiaxial loadings, as well as thermomechanical fatigue or aging.

Significant results in the characterization of adhesive joints were recently obtained for in the quasi-static loading regime, where a precise and complete experimental campaigns under multiaxial loading has been proposed for example in [1, 2]. However studies in the dynamic loading regime are less complete, they rely only on the single-lap joint specimen [5] or the double-lap joint specimen [6, 7]. These experimental set-up are dedicated only to the shear behavior of adhesive joints. Therefore, extensions to complex loading conditions combining

normal tension and shear are still limited. This is a considerable drawback for the description of real structures where the tensile dominate loading conditions control the overall joint strength. The importance of the tensile strength of joints has been already discussed in the pioneering papers like [3, 4]. Moreover, the real intrinsic constitutive behavior of polymers is nonlinear and combines hydrostatic and deviatoric components. A case of the yield strength depending of various parameters as described before is discussed in [8] for several examples. Recent studies of pressure sensitive adhesives and the influence of the pressure sensitive modelling on the evolution of different characteristics such as peak equivalent stress in the joint are [9–11]. [12] proposed a finite element implementation of a pressure sensitive yield criterion for adhesives.

Split Hopkinson bar systems are an established tool for characterizing materials and structures under dynamic loading. They provide global measurements: displacements and resultant forces at both ends of the specimen. However, in the case of an adhesive assembly, even though this technique enables to characterize the assembly, it does not provide local measurements in the neighborhood of the joint which would permit the identification of its behaviour, as already noticed in [5–7]. Therefore, additional local optical measurements are carried out and interpreted as displacements and strain fields using Digital Image Correlation (DIC) methods. For instance, DIC measurements have been performed under quasi-static conditions [13, 14] and under dynamic conditions [15–18].

In a previous work [19], we have shown that the measurements extracted from the experiment permit a rough estimate of the material parameters assuming some assumptions are verified. It has been shown that both global (SHPB) and local (DIC) measurements can be exploited to characterize main features of the material behavior of the adhesive joint. However, the complex geometry, as well as the inhomogeneous stress and strain states in the joint make a direct interpretation of measurements difficult. As a consequence, an accurate identification of the behavior of the adhesive joint can only be obtained by applying an inverse identification method.

The subject of inverse identification methods and in particular of constitutive parameters is supported by a large literature, as illustrated for example in [20–25]. General mathematical studies related to inverse methods such as existence, uniqueness and stability of the solution and the concept of ill-posed problems are reported for instance in [26, 27]. These sources present equally a framework for practical identification methods. An important complement to mathematical methods for inverse problems in the framework of Bayesian inference has been published in [28] and presents solution methods for controlling uncertainties both in the data and the parameter space.

Interesting reviews of different methods dedicated to the identification of constitutive parameter based on kinematic full-field measurements such as DIC have been recently proposed for example in [29, 30]. Several techniques are proposed within: the finite element model updating method (FEMU), the constitutive equation gap method (CEGM), the virtual fields method (VFM), the equilibrium gap method (EGM) and the reciprocity gap method (RGM).

The aim of this paper is the characterization of adhesive joints under dynamic multiaxial loadings. In previous studies [31, 19], we have proposed a novel specific sandwich specimen denoted as DODECA and performed simple material characterization using a Split Hopkinson Pressure Bar system and local strain measurements performed by Digital Image Correlation (DIC). Here, we add to this framework a detailed direct and inverse analysis of the system which will lead to the characterization of the yield and fracture surfaces in the space of equivalent von Mises stress vs hydrostatic stress. More precisely, we shall use a finite element model updating

method (FEMU) combined with a gradient free optimization method for the minimization of a cost function defined as the distance between measurements and model. Finally, precise qualitative tools are proposed for the uncertainties and confidence analysis of the identified parameters.

The paper is organized as follows. Section 2 makes a short hand-out of the experimental set-up. Section 3 discusses the direct numerical simulation of the experimental SHPB test based on the finite element method. The method is carefully broached as the method has to find the optimal compromise between computational time and accuracy, both aspects are required for the inverse minimization loop. Section 4 presents the framework of inverse identification method, the cost function and the minimization technique. Identification results, i.e. the constitutive material parameters, yield and fracture surfaces are discussed in section 5. They are later re-examined in the final section 6 from the point of view of the uncertainties.

2. Experimental set-up

The experimental apparatus, already discussed in [31, 19], consists of three main components, as displayed in figure 1:

(i) a conventional Split Hopkinson Pressure Bar (SHPB).

(ii) a specimen named *DODECA* enabling to test three distinct multiaxial loadings (denoted by 15°, 45° and 75°) with the same methodology and whose geometry has been optimized in order to avoid edge effects.

(iii) local measurements performed by Digital Image Correlation (DIC).

Therefore, information is provided either classically from global measurements on the Hopkinson bar system by using the DAVID software developed by [32], or from local optical measurements using a high-speed camera and a Digital Image Correlation (DIC) software to measure local displacements with a micrometric resolution, as described in [19].
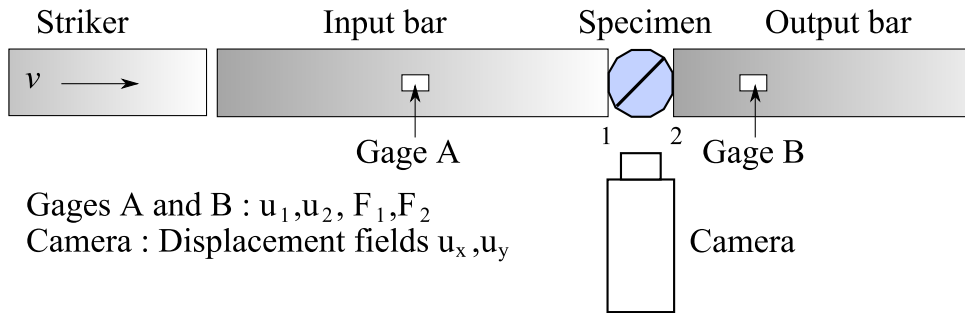

Figure 1: Experimental setup : the Split Hopkinson Pressure Bar, the DODECA specimen and the imaging system

The DODECA specimen is actually a sandwich dodecahedron, with two aluminum parts bonded by the adhesive joint. The outer flat edges are meant to ensure plane-to-plane contact between bars and the specimen in order to ease experimental and numerical procedures. The particular shape of the specimen enables three different impact angles (15°, 45° and 75°) leading to three different stress states in the adhesive joint. The adhesive joint is a 300 μm thick film bonded to aluminum parts of the specimen and passing between two nodes of the dodecahedron. Beaks are machined in the aluminum parts at the edges of the joint to avoid end effects such as strain or stress concentrations in the joint [1, 2, 33]. For more details on different specimen geometries and how the DODECA specimen has been designed, the reader is referred to [19].

3

3. Direct numerical simulation

The importance of the direct numerical simulation stems, on the one hand, from the complexity of the specimen and the loading conditions of the SHPB experiment, and on the other hand, from inverse identification method. As discussed below in section 4), the identification method is based on the iterative minimization of a cost function measuring the distance between the model and the measurements. Therefore, the direct numerical method should achieve an optimal compromise between accuracy and computation time.

3.1. Numerical strategy

Various modeling strategies of the SHPB test have been proposed. Analytic models relying on one-dimensional elastic wave propagation are widely used for the post-processing of the measured signals. Several studies based on analytic, closed-form models improve the interpretation of the signals. For instance, wave dispersion due to geometrical effects, i.e. a correction to consider the bar not as one-dimensional rod but as a three-dimensional object subjected to the Poisson effect, has been addressed [34]. Deconvolution techniques [35] have been developed in order to analyze signals on longer time intervals. A correction due to the punching of the specimen into the Hopkinson bars has been proposed [36]. The software DAVID [32], used for the direct interpretation of the global measurements of the SHPB gathers almost all the preceding analytic features for the computation of forces and displacements at any position of the input and output bars as well as the bar/specimen interfaces. In the case of simple cylindrical specimens of the same diameters as the bars, one can assume a homogeneous mechanical state within the specimen. Moreover, if balance of forces is ensured, i.e. equilibrium or forces at both ends of the specimen are similar, one can directly infer the mechanical behavior of the specimen. However, the main and most reliable outputs given by the DAVID software are force and displacement signals at any position in both bars. It is important to understand, that these force and displacement signals cannot be directly measured. They have to be computed from strain waves usually measured with strain gauges at the input bar (incident and reflected waves) and at the output bar (transmitted wave).

Numerical models have also been applied to tackle complex specimen design. Finite Element computations have been proposed in [37, 38] for the Brazilian disk specimen. Let us further mention, numerical modeling features are not based on consensus, despite the fact that FE computations of the SHPB test are widely used. When analyzing the SHPB set-up two extreme approaches have generally been used: (i) modeling of the specimen alone [38] and (ii) modeling of the complete SHPB system composed of the specimen and of the input and output bars [37, 7, 39].

Modeling of a stand-alone specimen is numerically simpler to develop and leads to shorter computation time. However, the contact boundary conditions between the bars and the specimen are replaced by either imposed displacements or pressure distribution. A precise simplification of the contact boundary condition is difficult and is usually accompanied by spurious reflected waves if the imposed boundary conditions are not perfectly consistent.

Modeling of the complete SHPB system overcomes the difficulty of the contact boundary conditions by modeling entirely the input and output bars. The loading boundary conditions of this computations are simply the input pulse (inferred from the strain gauges) at the beginning of the input bar and the free surface at the end of the output bar. This strategy is often preferred to the first one even if it conducts to longer computation. However, the contact boundary

conditions are still a critical difficulty, as the chosen contact model has a direct influence on the final results.

In this paper, we propose to model the complete SHPB system. However only small portions of the input and output bars are covered with 3D elements and the rest of the output bar is modeled with 1D elements. This hybrid model, permits on the hand side to ensure the computational accuracy around the contact between the bars and the specimens and to avoid spurious wave reflection and on the other hand side it decreases the computational burden.

This compromise has been justified in a small study by comparing the three different modeling strategies. The tested boundary conditions, the material parameters for the bars and the elastic-plastic material parameters for the adherents are displayed in tables 1,2 and 3, respectively. In order to avoid further complexity, a bulk DODECA specimen (without joint) instead of a sandwich DODECA aluminum specimen has been used for the study.

Table 1: Different FE models for the experimental setup

Condition	Input bar	Output bar
1	no	no
2	100 mm (3D)	100 mm (3D)
3	100 mm (3D)	100 mm (3D)+1.4 m (1D)
4	3 m (3D)	1.5 m (3D)

Table 2: Material parameters for the elastic bars

Diameter	D_B	(mm)	40
Young's modulus	E_B	(GPa)	74.5
Poisson coefficient	ν_B	(-)	0.33
Density	ρ_B	(kg/m^3)	2820

Table 3: Material parameters for the elastic-plastic adherents

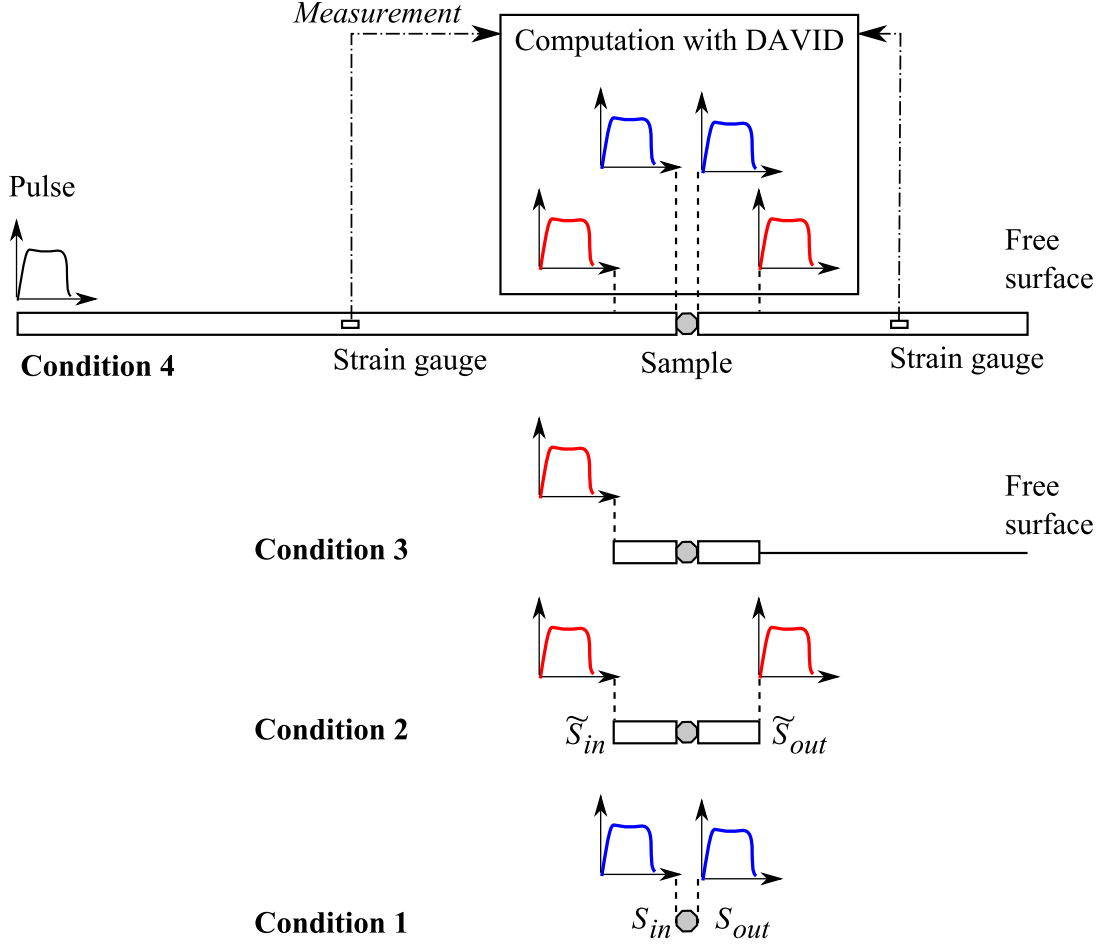| Young's modulus	E_A	(GPa)	72
Poisson coefficient	ν_A	(-)	0.33
Density	ρ_A	(kg/m^3)	2800
Yield stress	σ_A^0	(MPa)	260
Yield stress at 4%	σ_A^1	(MPa)	380

Figure 2: Numerical strategies for the modeling of the DODECA experiment based on the four conditions of table 1. Condition 1 : no bars, Condition 2 : bars of 100 mm, Condition 3 : bars of 100 mm + an output beam, Condition 4 : bars of 3 m and 1.5 m

The computations were performed using ABAQUS [40] with an explicit time integration scheme. Time increments were automatically adapted as a function of stability and convergence criteria. The meshes used for the different numerical strategies are displayed in figure 3. These meshes are rather coarse as the purpose of the study is only to determine the numerical strategy by comparing three modeling strategies. Results are not meant to be used to identify material parameters as in section 3.3. There are 1680 volume elements (C3D8R) for the DODECA specimen alone and there are 3686 volume elements (C3D8R) for the DODECA specimen with the small portions of bars. In addition there are 35 beam elements (B31) for the 1D portion of the output bar.. Let us denote by (S_{in}, S_{out}) and $(\widetilde{S}_{in}, \widetilde{S}_{out})$ the input and output surfaces on the specimen and on the bars respectively, as depicted in figure 2. Let us remark that Condition 4 corresponds to a complete 3D of the SHPB system and will therefore be considered as the reference computation. Condition 2 is an attempt to reduce computation time by truncating both the input and output bars and imposing at $\widetilde{S}_{in}$ and $\widetilde{S}_{out}$ the corresponding measured displacements. For comparison of the numerical computations, we used a real experiment with a DODECA specimen without adhesive joint. More precisely, comparison was done on the displacements at (S_{in}, S_{out}) and $(\widetilde{S}_{in}, \widetilde{S}_{out})$. For the experimental displacements, we used the displacements provided by the software DAVID, which converts the strain measurements at the gauges into displacement and force signals anywhere in both the input and output bars.

6

A comparison between the experimental forces (with the punching correction) and numerical computations of condition 1 inferred at S_{in} and S_{out} is presented in figure 4. One can remark the good qualitative agreement between computations and measurements. More precisely, the overall response has similar shape and amplitude and oscillations due to several reflections at the free surfaces of the DODECA specimen are in phase. However, the discrepancies are still important to be used within an inverse identification procedure.

(a) Condition 1

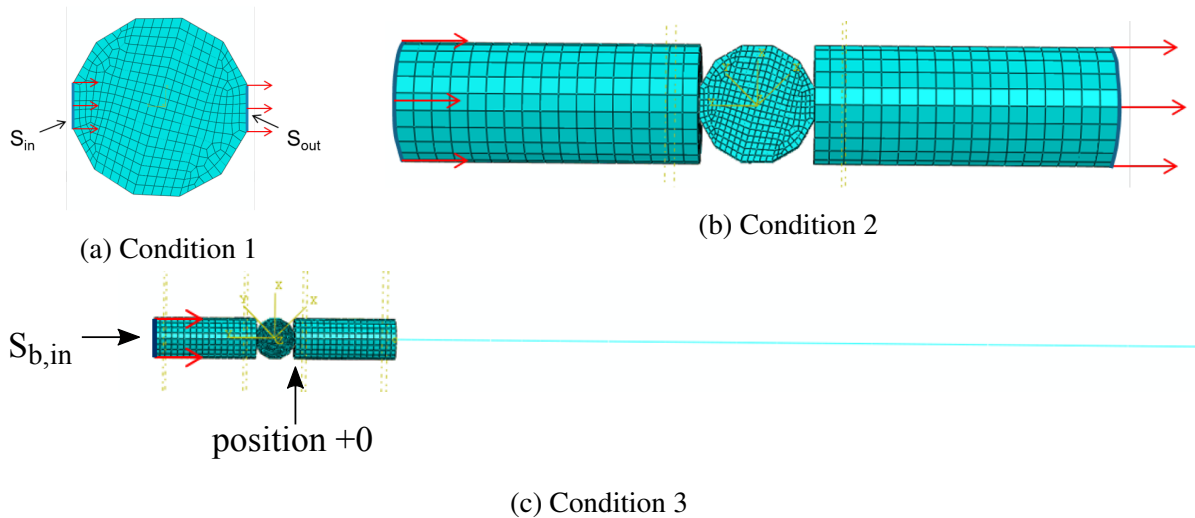(b) Condition 2

(c) Condition 3

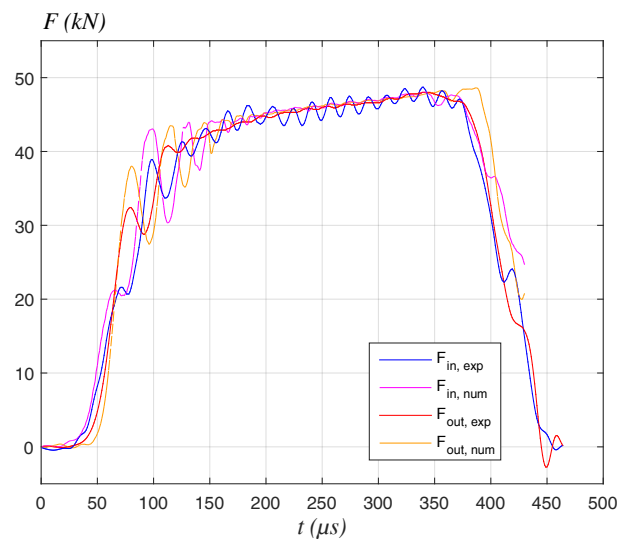Figure 3: Meshes used for the numerical strategies : condition 1, 2 and 3 of table 1

Figure 4: Time evolution of the input and output forces (at the specimen/bar interfaces) : comparison between the experiment and the FE computation (condition 1)

The first comparison involves two numerical simulations, one with the complete bars (condition 4) and one with bars having a reduced length (condition 2). The comparison is performed by imposing the numerical obtained displacements at $\widetilde{S}_{in}$ and $\widetilde{S}_{out}$ in the computation with condition 4 as the boundary input of the computation in condition 2. Figure 5) displays the

comparison of conditions 2 and 4 as a time evolution of the input and output forces. One can remark that both the overal behavior and the oscillations are very similar. Here the imposed displacements on $\widetilde{S}_{in}$ and $\widetilde{S}_{out}$ for the computation with condition 2 were extracted from the computation of condition 4. This result shows, that it is possible to reduce the modeled part of the bars without losing accuracy. Moreover, it validates that 100 mm long bars are sufficient to capture accurate signals. This simplification rises however several difficulties. If the imposed displacements on $\widetilde{S}_{in}$ and $\widetilde{S}_{out}$ in condition 2 do not stem from the numerical simulation with condition 4 but directly from the experiment, significant oscillations occur $\widetilde{S}_{out}$ and have an increasing amplitude over time as exhibited in figure 6. It shows that the imposed displacements at $\widetilde{S}_{in}$ and $\widetilde{S}_{out}$ extracted from the experiment are not perfectly in phase with the computed waves, which generates unrealistic reflections. This phenomenon is due to the discrepancy between simulated and real wave propagation. This limitation also holds for condition 1.
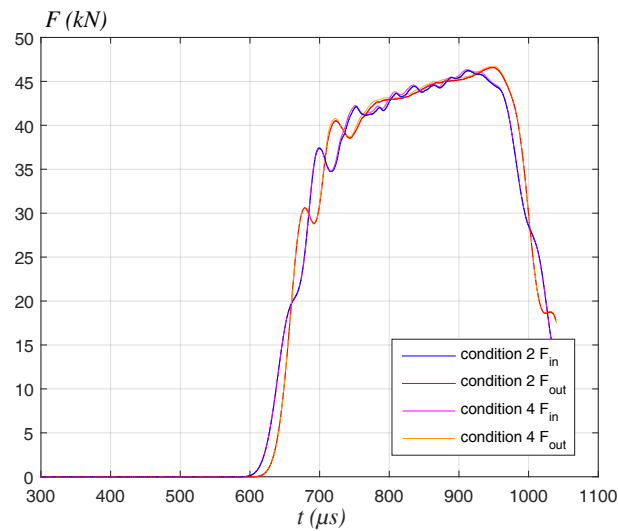

Figure 5: Time evolutions of the input and output forces (at the specimen/bar interfaces) : comparison between conditions 2 and 4
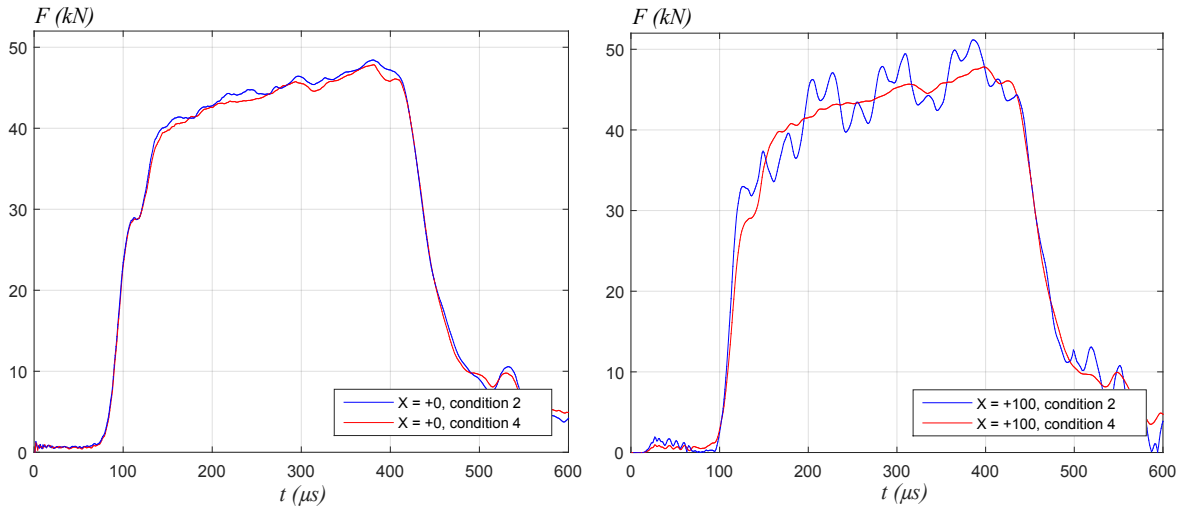
Figure 6: Time evolutions of the output force at the specimen/bar interface (left) and at 100 mm from the interface : comparison between conditions 2 and 4. Boundary conditions for the Condition 2 are extracted directly from an experiment : Reflections issues

The idea proposed next, is to take advantage of the FE model of condition 2 but overcoming reflection issues if the imposed displacements are not perfectly consistent with numerical wave propagation, by adding 1D elements for the rest of the output bar as shown in figure 3c. Thus, boundary conditions are imposed only at $\widetilde{S}_{in}$ and the wave propagates freely through the output bar until it reaches the free surface at the end of the bar where a reflection takes place as for real bars. Thus, oscillation issues are overcome as shown in figure 7. Different numerical strategies are summarized in figure 2.
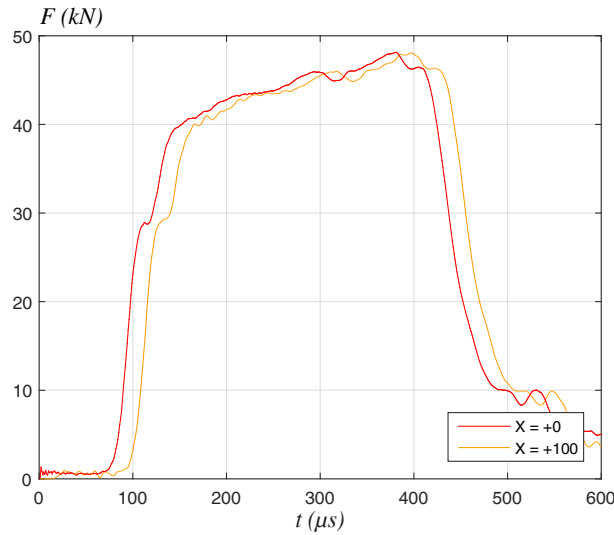

Figure 7: Time evolution of the output force extracted at the specimen/bar interface (X = +0) and at 100 mm from the interface (X = +100) with Condition 3: Solving reflection problems

3.2. Contact law

Another critical feature of the numerical computation is the contact model. Several different theoretical and numerical modeling options are available. Let us further refer to the classic

9

penalization method, which relates the interpenetration distance between the surfaces in contact and the corresponding contact pressure. Specifically it supposes a zero pressure in the absence of contact and an increasing pressure with interpenetration. The contact law depends of the roughness profiles and explicit empirical formulas for the pressure function have been proposed in the literature, as for example [41–43]. Contact laws relating nominal surface interpenetration and the resulting contact pressure can be inferred from such empirical works. Next, we propose to define the contact law as a piecewise linear function of the pressure as a function of the interpenetration using three adjustable parameters (c_1, P_1, P_2), as displayed in table 4.

Table 4: Contact law

Interpenetration (mm)	Contact pressure (MPa)
0	0
c_1	P_1
1	P_2

3.3. Numerical simulation of SHPB tests with adhesive joints

The direct numerical model of the SHPB test including the sandwich DODECA specimen with adhesive joint is depicted in figure 9. The mesh size has been refined in comparison to section 3.1 in order to capture more accurately strain gradients for the inverse method. The mesh is composed of 159776 volume elements (C3D8R) for each small portion of the bars and 7170 volume elements (C3D8R) for each substrate of the DODECA specimen, in addition there are 48 beam elements (B31) for the 1D portion of the output bar and 400 joint elements (C0H3D8) for the adhesive joint. The typical mesh size for the DODECA specimen and bars is 1 mm. It has been checked that results are not sensitive to the mesh pattern for the tested conditions. Moreover, a convergence study has been conducted to justify the chosen mesh density. The force at the surface S_{out} is presented in figure 8a for various mesh sizes of the DODECA specimen (modeled alone). Convergence is obtained for a typical mesh size of 1 mm as no significant variation is observed with finer mesh density. Moreover, the force at the surface $\widetilde{S}_{out}$ is presented in figure 8b for various mesh sizes of the bars considering that the DODECA specimen is modeled with elements of typical size of 1 mm. Convergence is also obtain for the same mesh density.

(a) Mesh convergence of the specimen.
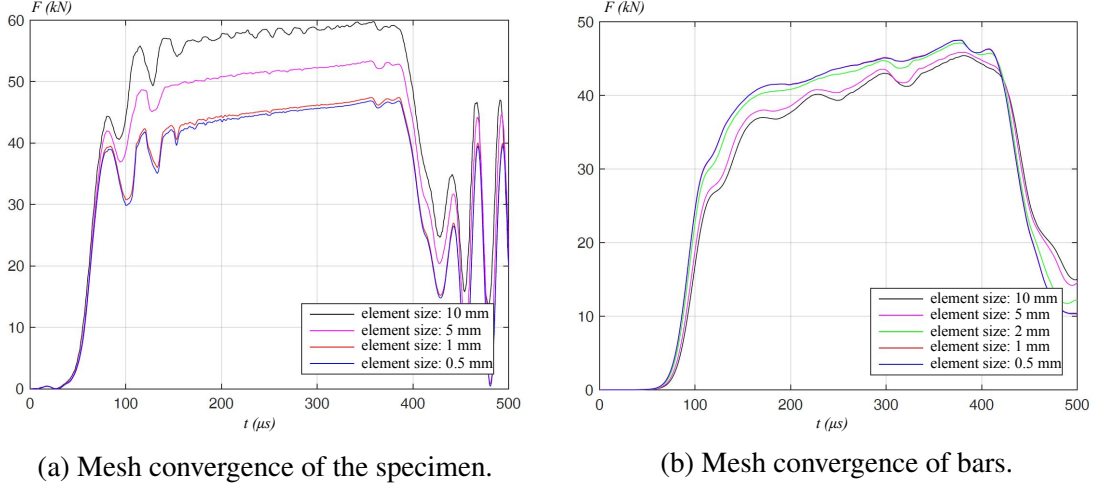
(b) Mesh convergence of bars.

Figure 8: Mesh density.

Bars are purely elastic and the adherents of the specimen are elastic-plastic with a piecewise linear isotropic hardening curve. The two adherent parts of the specimen are made of aluminum whose elastic parameters are relatively well known. The corresponding geometrical and material parameters are listed in table 5.

Let us now mention that the experiments with plain specimens revealed that the plastic parameters present some variability even within the same material batch. The parameter variability is probably the signature of the process, sample history as it depends on the rolling direction, on the specific plate or the orientation of the specimen, etc. . Therefore particular dynamic tests have been performed in order to identify material parameters of the aluminum. When manufacturing the corresponding specimens, particular care was given to the sample extraction from the same rolled plate along the same direction as the adherent of the DODECA specimen.

The adhesive joint is assumed to be elastic-plastic with a piecewise linear isotropic hardening. As a consequence, five material parameters have to be identified, namely: (i) the Young's modulus denoted by E_J, (ii) the Poisson ratio ν_J, (iii) the initial yield stress σ_J^0, (iv) the yield stresses σ_J^j and (v) the corresponding fixed plastic strains ε_J^j, where the subscript J stands for *joint* and $1 \leq j \leq 2$. Thus, the 5-dimensional parameter space is denoted by:

$$\Theta = \left\{ \left(E_J, \nu_J, \sigma_J^0, \sigma_J^j \right), \ (1 \leq j \leq 2) \right\} \tag{1}$$

Let us finally highlight, that both the adherents and the adhesive joint of the specimens are represented using elastic-plastic material in the conditions of the test. However, the material coefficients are highly different as dictated by the characteristics of aluminum and the polymer joint respectively and that they are not related in any other matter. Moreover, the behavior of the aluminum adhesives is identified independently and will therefore not interfere with the characterization of the joint.
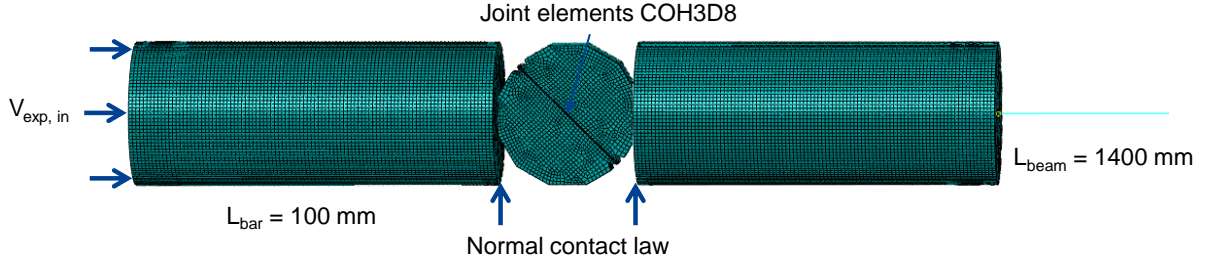
Figure 9: Numerical mesh for the experimental SHPB set-up with the DODECA specimen at 45°.

DODECA specimen			
Inscribed circle diameter	d	(mm)	40
Thickness	*th*	(mm)	10
Adherent Young's modulus	E_A	(GPa)	72
Adherent Poisson ratio	v_A	(-)	0.33
Adherent density	ρ_A	(kg/m^3)	2800
Adherent yield stress	σ_A^0	(MPa)	235
at 0.41%	σ_A^1	(MPa)	290
at 5%	σ_A^2	(MPa)	410
Adhesive joint thickness (depends on each specimen)	th_j	(mm)	≈ 0.3
Adhesive joint length	L_j	(mm)	38.65
Adhesive joint density	ρ_j	(kg/m^3)	1100
Bars modeled with 3D elements			
Diameter	D_B^{3D}	(mm)	40
Length	L_B^{3D}	(mm)	100
Young's modulus	E_B	(GPa)	72.31
Poisson ratio	v_B	(-)	0.33
Density	ρ_B	(kg/m^3)	2802
Output bar modeled with 1D elements			
Diameter	D_B^{1D}	(mm)	40
Length	L_B^{1D}	(mm)	1400

Table 5: Geometrical and material parameters of the experimental SHPB set-up

4. Inverse method

4.1. Cost function and minimization space

In the preceding section 3, we defined both the direct Finite Element simulation of the experimental SHPB set-up and the set of material parameters for the joint:

$$\boldsymbol{\theta} = \left(E_J, v_J, \sigma_J^0, \sigma_J^j \right)$$

which has to be identified. Supplying the direct problem with a compatible parameter set θ transforms the problem into a well-posed direct problem which can numerically be solved and which provides the complete history of the mechanical fields of the set-up. The inverse

identification problem seeks to find the parameter vector $\boldsymbol{\theta} \in \Theta$, which minimizes the distance between measured and computed quantities, defined by the cost function

$$\varphi : \boldsymbol{\theta} \in \Theta \mapsto \varphi(\boldsymbol{\theta}) \in \mathbb{R}^+$$

In order to define the cost function, *global* and *local* measurements are exploited next.

The classic interpretation of strain waves measurements at the SHPB tests provides global displacements and forces at any position of the bars, which can further be used as a measurement value in the definition of the cost function. Next, the superscript $SHPB$ will refer to *global* measurements from this strain wave interpretation. Thus, the displacement signal at $\widetilde{S}_{in}$, further also denoted as U^{SHPB} is used as an input boundary condition of the direct problem detailed in the preceding section 3. As a consequence, the output force signal F^{SHPB} at $\widetilde{S}_{out}$ is used as a *global* measurement in the definition of the cost function φ. This output force signal F^{SHPB} is extracted from the direct FE computation with the same frequency as measurements, more precisely every μs or at $f^{SHPB} = 1$ MHz rate.

The *local* measurements refer to local values of the mechanical fields as measured through optical means and DIC post-processing. For example, shear and normal displacements at the center of the adhesive joint are measured by DIC and are used as *local* measurements in the definition of the cost function φ. Next, the superscript DIC will refer to these *local* measurements. More precisely, we are going to use the tangential displacement jump ΔU^{DIC}, corresponding to the shear loading and the normal displacement jump ΔV^{DIC} corresponding to the normal loading. These quantities are computed by measuring the displacement difference between two positions in the aluminum adherents at precisely 1.3 mm above and under the midline of the adhesive joint. For example, the comparison of histories of computed and measured *local* displacements signals is presented for a test at 45° in figure 10.

The final complete expression of the cost function to be minimized is given by the following combination of measures:

$$\varphi(\boldsymbol{\theta}) = \alpha \left\| F^{SHPB} - F^{FEM}(\boldsymbol{\theta}) \right\| + \beta \left\| \Delta U^{DIC} - \Delta U^{FEM}(\boldsymbol{\theta}) \right\| + \gamma \left\| \Delta V^{DIC} - \Delta V^{FEM}(\boldsymbol{\theta}) \right\| \quad (2)$$

where $\alpha, \beta, \gamma \in \mathbb{R}_+$ are positive weights and $\|\cdot\|$ is the standard vector norm. The precise values of the weights is adapted to the amplitudes and the noise intensities of the different signals. The choice used in the following analysis, corresponds to $\alpha = 1/F_{max}^{SHPB}$, where F_{max}^{SHPB} is the maximum value of F^{SHPB}, and $\beta = \gamma = 100$ μm^{-1}. These values account for the difference in frequency acquisition of the signals and therefore different vector lengths. More precisely, the global force F^{SHPB} is measured with 13 times higher acquisition frequency than displacement jumps ΔU^{DIC} and ΔV^{DIC}. Moreover, considering that the amplitude of ΔU^{DIC} is around 20 times higher than the amplitude of ΔV^{DIC}, the condition $\beta = \gamma$ means that the jump measurement ΔV^{DIC} has a limited weight in the minimization process. This choice is justified by the better signal-to-noise ratio of the displacement jump ΔU^{DIC} than that of ΔV^{DIC}. However, in the case of a 75° loading condition, γ is increased to 200 μm^{-1} to account for a higher amplitude of ΔV^{DIC} in this particular loading.
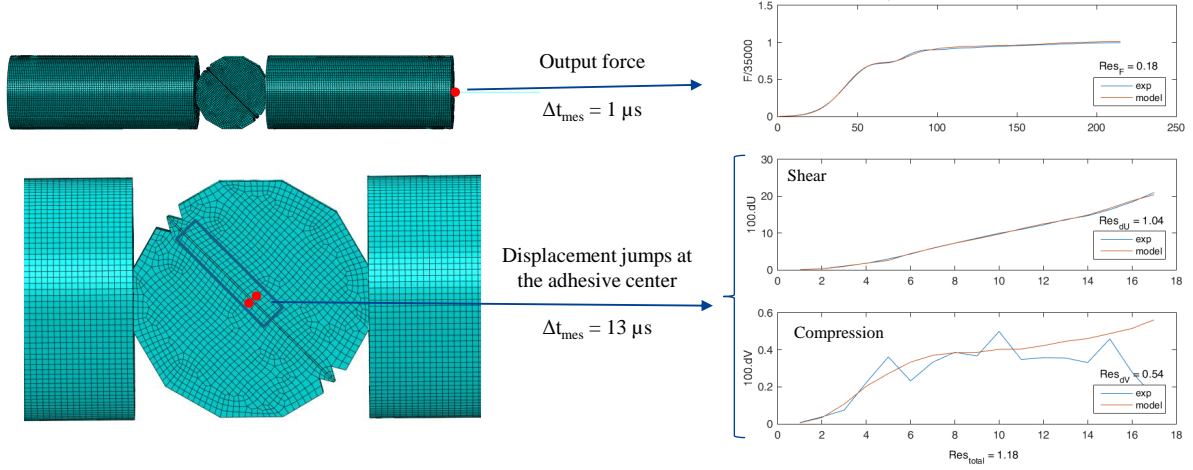
Figure 10: Extraction of computed signals $F^{FEM}, \Delta U^{FEM}, \Delta V^{FEM}$ and comparison with measurements $F^{SHPB}, \Delta U^{DIC}, \Delta V^{DIC}$

The inverse method consists in solving the following minimization problem:

$$\boldsymbol{\theta}^I = \underset{\boldsymbol{\theta} \in \Theta}{\operatorname{argmin}} \left[\varphi(\boldsymbol{\theta}) \right] \qquad (3)$$

under the constraint that $F^{FEM}, \Delta U^{FEM}, \Delta V^{FEM}$ are extracted from the direct FE model presented in section 3 and, therefore, depends on the trial material parameters of the adhesive joint $\boldsymbol{\theta} \in \Theta$.

The numerical minimization is performed using a gradient-free Nelder-Mead descent algorithm programmed in Python [44] script. At each iteration of the minimization loop, denoted within the fields and parameters by the index k, the current evaluation $\boldsymbol{\theta}_k$ is sent to Abaqus [40] to compute the output signals $F^{FEM}(\boldsymbol{\theta}_k), \Delta U^{FEM}(\boldsymbol{\theta}_k), \Delta V^{FEM}(\boldsymbol{\theta}_k)$. Then, these quantities are sent back to the Python script for the evaluation of the cost function $\varphi(\boldsymbol{\theta}_k)$ and the proposal of a new trial parameter set $\boldsymbol{\theta}_{k+1}$. Iterations are computed until convergence, as depicted in figure 11. Among the large variety of gradient-free algorithms (genetic, particle swarm, Nelder-Mead etc.), the Nelder-Mead simplex algorithm has been chosen as it is well indicated for local minimum search within a multi-dimensional context. This algorithm converges to the nearest optimal point, which seems sufficient as the initial guess is educated from a priori knowledge of the studied materials. Other algorithms such as particle swarm optimization [45] (e.g., applied to tailor material properties [46]) do not stop in local minimum but often necessitate a sufficiently large number of particles inducing larger number of calls to the cost function than the Nelder-Mead algorithm, which would be computationally costly.
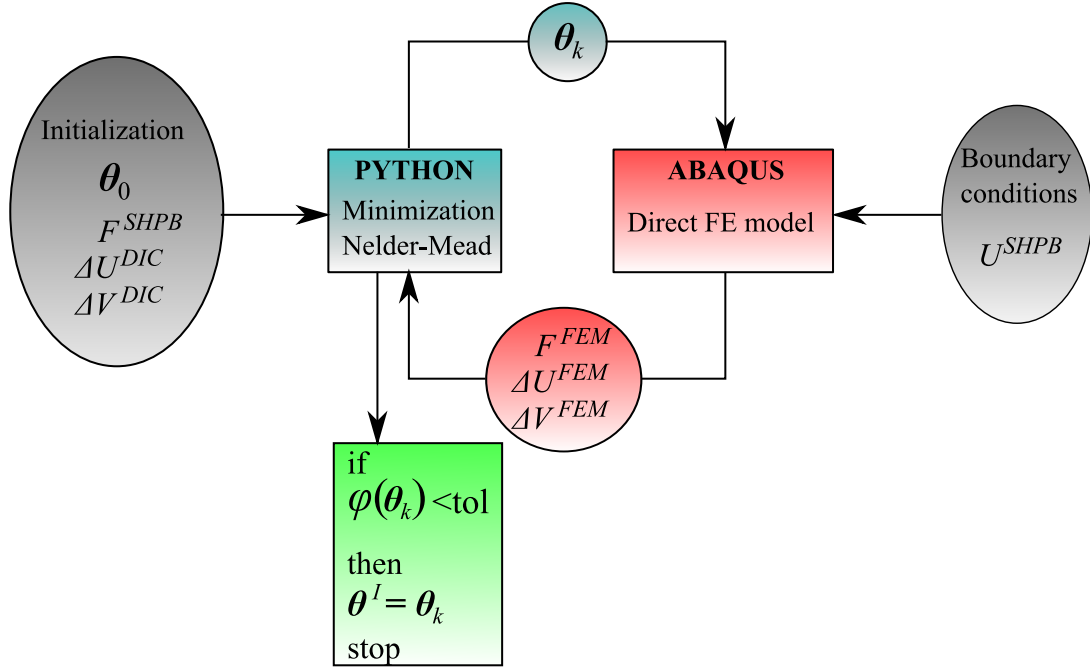
Figure 11: Schematic representation of the inverse method

Despite the very simple descent algorithm and standard FEM computations combined in the algorithm, several difficulties can be encountered.

As local and global measurements are mixed, combining the standard wave interpretation and DIC respectively, it is of utmost importance to synchronize consistently the time origin of each of the different signals. The synchronization is done as follows. Let us consider Δt^{SHPB} and Δt^{DIC} the two time shifts enabling to synchronize the SHPB and DIC measurements with computations as shown in figure 10. The determination of Δt^{SHPB} and Δt^{DIC} is done in two steps: first, (i) an approximate evaluation of the adhesive joint material parameters is made following the experimental method proposed by [19], and then, (ii) a direct computation is performed with the first estimation of the parameters. The shifts Δt^{SHPB} and Δt^{DIC} are now computed directly from the comparison of experimental and numerical signals. Let us further remark that, Δt^{DIC} is more difficult to estimate due to the limited frequency of acquisition of the optical system.

Contact properties between the bars and the specimen also influence the outcome of the minimization process. Without a precise a priori knowledge of the parameters, contact parameters c_1, P_1, P_2 defined in table 4 have equally been included in the minimization procedure because the contact behavior depended on each test.

In this case, the minimization space defined by (1) is therefore extended to the 8-dimensional space:

$$\Theta = \left\{ E_J, \nu_J, \sigma_J^0, \sigma_J^1, \sigma_J^2, c_1, P_1, P_2 \right\} \tag{4}$$

In this case, the strain yield limit, i.e. plastic strains corresponding to σ_J^1 and σ_J^2 are fixed manually in the minimization algorithm. Although plastic strains are negligible in the adherents for the 45° and 15° loading conditions , significant plastic strains take place in the aluminum adherents, for the 75° loading condition. Therefore, results significantly depend on plastic properties of the aluminum for the 75° loading condition. As already mentioned, plastic properties of the aluminum adherents present some variability even within the same lot depending on the rolling

direction or the specific plate and introduce a bias between different tests. Therefore, additional plasticity parameters have been added to characterize the yield surface for 75° loading condition, the yield stress σ_A^0 and σ_A^1 at 5% strain of the aluminum adherents. The parameter space (1) for the 75° loading condition becomes therefore:

$$\Theta = \left\{ E_J, \nu_J, \sigma_J^0, \sigma_J^1, c_1, P_1, P_2, \sigma_A^0, \sigma_A^1 \right\} \tag{5}$$

Fracture properties are not determined using the inverse identification method by the minimization of the cost function φ. They are directly obtained as the failure stresses and presented as a surface in the space of von Mises equivalent stress vs hydrostatic stress. When fracture is observed experimentally, the stress state is extracted from the direct FE simulation at the corresponding time.

4.2. Ill-posedness and regularization

Inverse methods are ill-posed, meaning that solutions tend not to be unique and that small errors in the input data might correspond to large differences in the identified parameters. The techniques applied to decrease this effect, modify the convexity and the smoothness of the cost function by adding an additional term and are denoted as regularization. For instance, one can add a term of the form $\left\| \theta - \theta^{est} \right\|$ where θ^{est} is a reasonable, expected value of the material parameters given as a prior *estimation*. A similar effect is obtained by adding a constraint such as $\left\| \theta - \theta^{est} \right\| \leq \eta$, where η quantifies the range of the parameter set and will constrain the solution around the a prior *estimation*. These regularization techniques tend to select one solution on the basis of additional knowledge such as a rough estimation of material parameters as proposed by [19]. In this contribution, the regularization has not been applied automatically. However, material parameters have been manually chosen among several solutions obtained with different initial parameter vectors θ_0 and different fixed choices of plastic yield strains ε_J^1 and ε_J^2, corresponding to σ_J^1 and σ_J^2 respectively, in the minimization algorithm.

In addition, the dimension 8 of minimization space $\Theta \in \mathbb{R}^8$ complicates further the minimization procedure. Thus, not all dimensions of the minimization space are explored at the same time. The minimization process is orientated to determine, first, the elastic parameters by focusing on the initial part of the signals, where the material behavior is assumed to be purely elastic. Consequently, only the first 4 images, corresponding to the first 50 µs are considered for the preliminary elastic identification of E_J, ν_J. Then, remaining material parameters are identified by performing the optimization on the complete signals considering E_J, ν_J fixed at the previously identified values.

Finally, the failure stresses are identified by extracting the corresponding stress state from the direct FE simulation just as fracture is observed experimentally.

5. Results

The material parameters and fracture properties identified for each loading condition 15°, 45° and 75°are listed in tables 6, 7 and 8 respectively.

Let us first remark that the values identified are consistent with standard accepted values of parameters in structural adhesive joints. For instance, the adhesive joint under scrutiny has a Young's modulus of 1400 MPa in quasi-static conditions and therefore the values of 2100 MPa and 2300 MPa identified in dynamic conditions are consistent with this information.

16

Similar remarks apply to other parameters. An important role in this result is played by the regularization performed during the minimization process and discussed in the previous section.

Discrepancies of contact parameters between loading conditions are not fully understood, but may be due to rigidity and geometry differences of the specimen for each angle condition.

Figures 12, 13 and 14 present comparisons between measurements and corresponding computations. The figures show that the three quantities $F, \Delta U, \Delta V$ are correctly modeled in an acceptable uncertainties range. This will be discussed in the next section.

In addition, the results obtained for the three loading conditions are gathered to construct a yield surface and a fracture surface in two different spaces as presented in figure 15. The first space is made up of normal stress and shear stress in the adhesive joint and the second one of von Mises equivalent stress and hydrostatic stress in the adhesive joint. The yield surface is consistent with typical mechanical properties of structural adhesive joints. For instance, the yield stress increases with the hydrostatic pressure (Drucker-Prager type behavior) and decreases when the adhesive joint is under tension. The rupture surface is similar to the yield surface with slightly higher values. As we know plastic deformation is important, it would be interesting to build a mixed criterion with both stress and strain.

Table 6: Identified material parameters for 45° loading conditions

	Adhesive joint						Contact		
	E_J	ν_J	σ_J^0	σ_J^1	ε_J^1	σ_J^2	ε_J^2	c_1	P_1	P_2
Test	(MPa)	(-)	(MPa)	(MPa)	(-)	(MPa)	(-)	(µm)	(MPa)	(MPa)
1	2100	0.42	106.5	115	0.18	142	2	0.014	315	1000
2	2100	0.42	99.5	114	0.11	148	2	0.012	330	900

Table 7: Identified material parameters for 15° loading conditions

	Adhesive joint						Contact		
	E_J	ν_J	σ_J^0	σ_J^1	ε_J^1	σ_J^2	ε_J^2	c_1	P_1	P_2
Test	(MPa)	(-)	(MPa)	(MPa)	(-)	(MPa)	(-)	(µm)	(MPa)	(MPa)
1	2100	0.42	85	97	0.04	120	1.7	0.016	555	3000

Table 8: Identified material parameters for 75° loading conditions

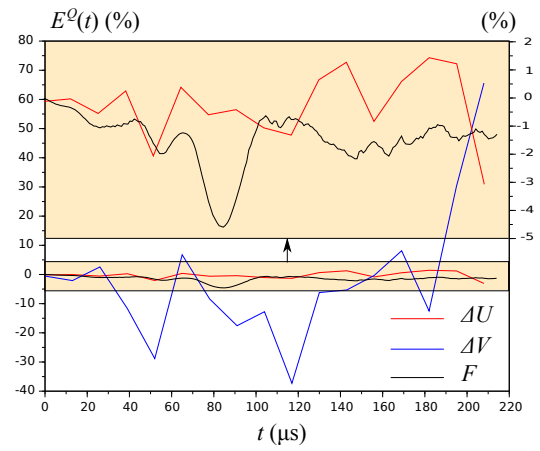|	Adhesive joint					Contact			Aluminum adherents	
	E_J	ν_J	σ_J^0	σ_J^1	ε_J^1	c_1	P_1	P_2	σ_A^0	σ_A^1 at 5%
Test	(MPa)	(-)	(MPa)	(MPa)	(-)	(µm)	(MPa)	(MPa)	(MPa)	(MPa)
1	2300	0.42	142	204	2	0.019	580	3000	255	870
2	2300	0.42	145	252	2	0.018	560	3100	260	880
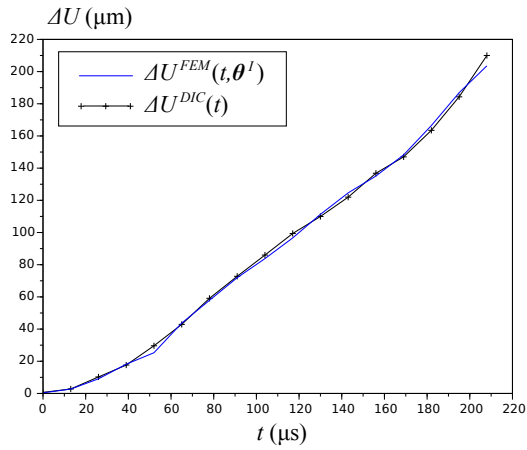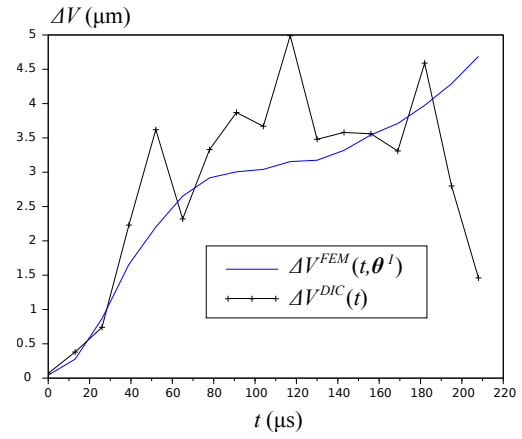
17

(a) Measured and computed signals: ΔU

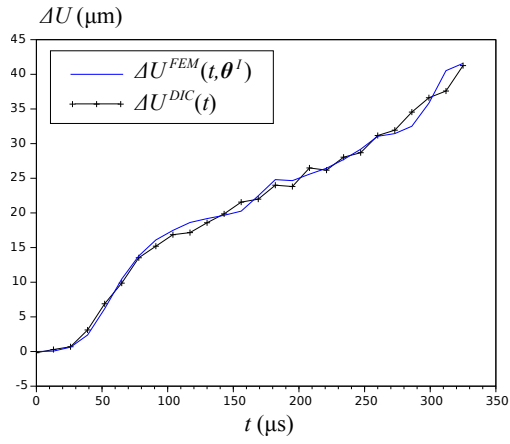(b) Measured and computed signals: ΔV
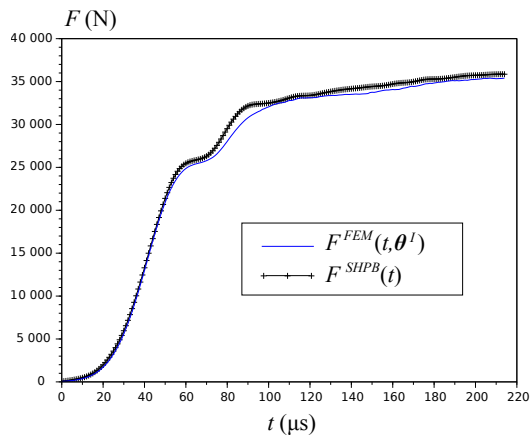
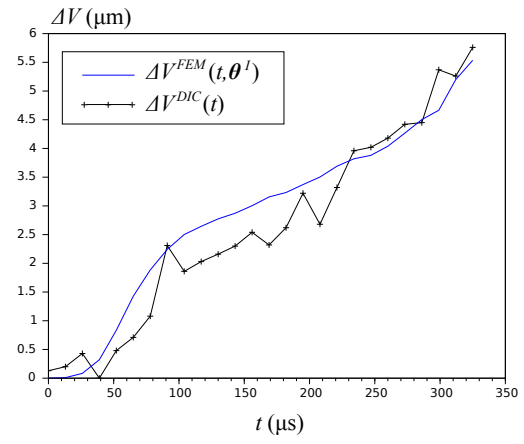(c) Measured and computed signals: F
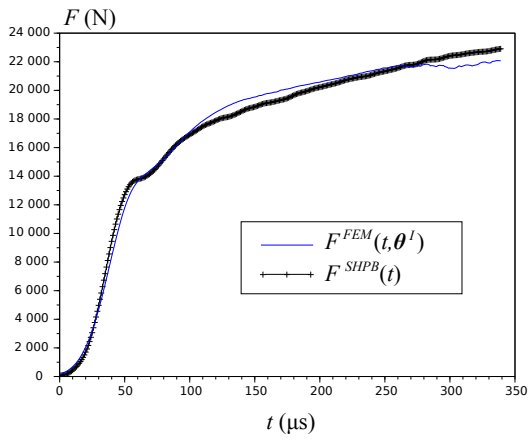
(d) Reconstruction error

Figure 12: Measured and computed signals for the 45° loading condition

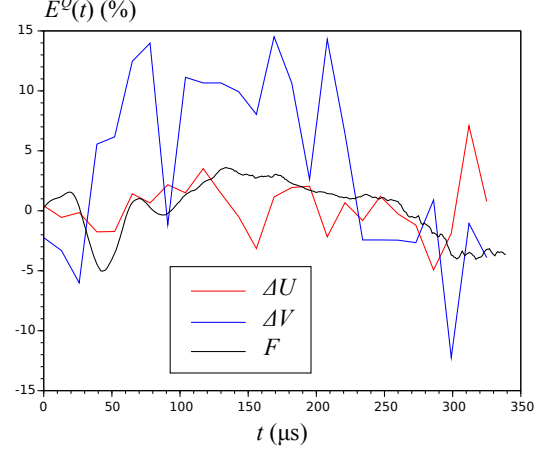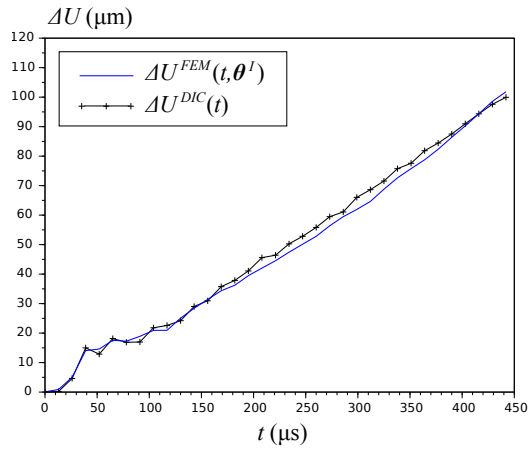(a) Measured and computed signals: ΔU

(b) Measured and computed signals: ΔV
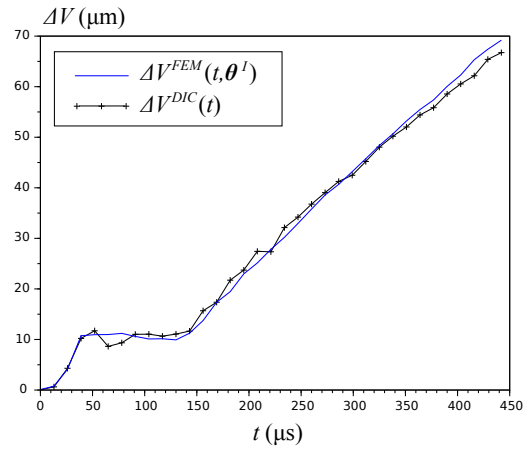
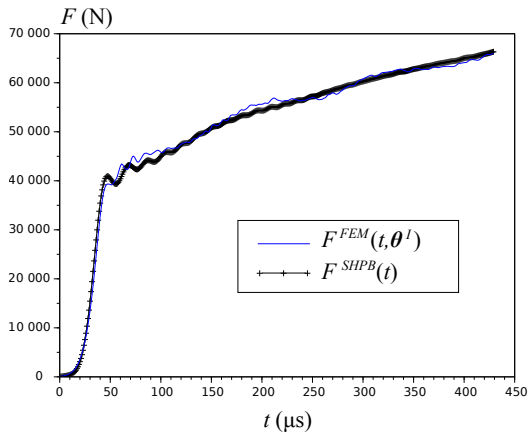(c) Measured and computed signals: F

(d) Reconstruction error

Figure 13: Measured and computed signals for the 15° loading condition

(a) Measured and computed signals: ΔU

(b) Measured and computed signals: ΔV

(c) Measured and computed signals: F

(d) Reconstruction error

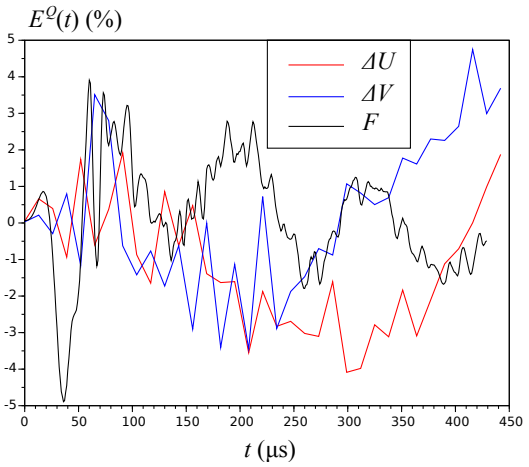Figure 14: Measured and computed signals for the 75˚ loading condition
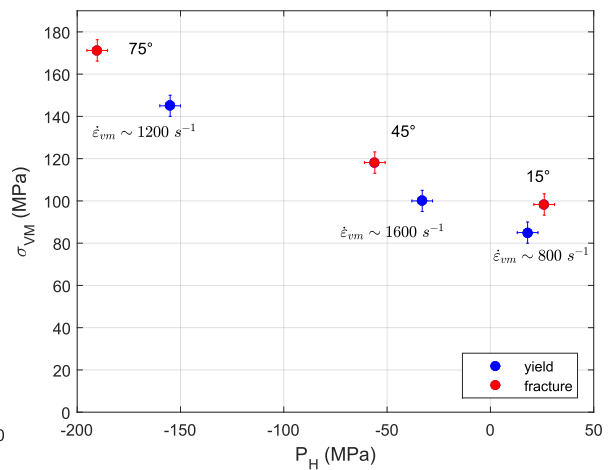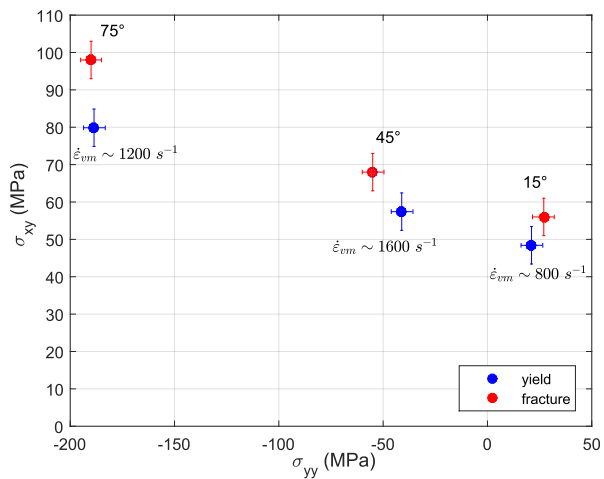

Figure 15: Yield and fracture surfaces : space of normal and shear stresses (left), space of von Mises equivalent stress and hydrostatic stress (right)

20

6. Qualitative estimation of uncertainties

Measurement uncertainties and uncertainties resulting from the identification procedure (modeling choices, sensitivity of the direct numerical model) should be estimated (at least qualitatively). Measurement uncertainties depend on the measurement system (i.e., DIC or SHPB). The uncertainty amplitude is roughly evaluated to around 2.5 μm for the DIC measurement system. This estimation is done by analyzing ΔV^{DIC} in figure 12b because the signal amplitude is very low and measurement uncertainties are visible. A simple polynomial function is fitted on measurements ΔV^{DIC} (through a least square method) in order to extract an estimation of uncertainties δ^{DIC} as shown in figure 16. The relative uncertainty is denoted by $\zeta^{\Delta U}$ or $\zeta^{\Delta V}$ and defined as the amplitude of the measurement noise δ^{DIC} (an upper bound is considered: 2.5 μm) divided by the amplitude of the corresponding signal ΔU^{DIC} or ΔV^{DIC} (as defined by (9)). Resulting relative measurement uncertainties are listed in table 9. Relative uncertainty ζ^F related to the wave analysis of the SHPB system is fixed arbitrarily to 3%, that is a reasonable upper bound.
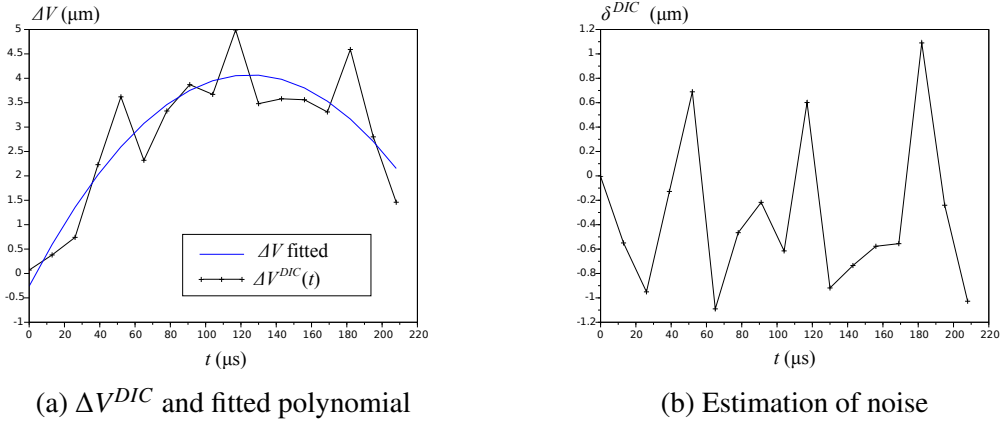

(a) ΔV^{DIC} and fitted polynomial   (b) Estimation of noise

Figure 16: Estimation of measurement uncertainties for DIC : example of the signal ΔV^{DIC} at 45°

Table 9: Estimation of measurement uncertainties for $F, \Delta U, \Delta V$ for the three different loading conditions

Condition	$\zeta^{\Delta U}$ (%)	$\zeta^{\Delta V}$ (%)	ζ^F (%)
45°	1	51	3
15°	6	44	3
75°	3	4	3

The identification performed in this work has been developed with a purely deterministic nature, therefore, the results are not presented as probability density functions. However, a qualitative estimation of the errors on the identified material parameters can be performed. Let us remark that uncertainties appear not only as an outcome of the measurement procedure, but equally as an outcome of the bias introduced by the inverse method itself. This is partly due to the differences between the real experiment and the direct FE model. The later will always be a rather simpler model than the complex reality. Indeed, modeling choices such as the

elastic-plastic behavior for the adhesive joint, the isothermal conditions, the unilateral contact law (without friction effects) are responsible for a residual distance between measurements and computed signals. Consequently, the cost function φ, which measure the difference between model and reality, cannot rigorously vanish, i.e. $\varphi(\boldsymbol{\theta}^I) > 0$ where $\boldsymbol{\theta}^I$ denotes the identified optimal material parameter vector.

The residual *error* is quantified as follows:

$$E^Q(t) = \frac{Q(t, \boldsymbol{\theta}^I) - Q(t)}{[Q(t)]_T} \tag{6}$$

where $Q(t)$ is a measured signal:

$$Q(t) \in \left\{ \Delta U^{DIC}(t), \Delta V^{DIC}(t), F^{SHPB}(t) \right\} \tag{7}$$

where $Q(t, \boldsymbol{\theta})$ is a computed signal:

$$Q(t, \boldsymbol{\theta}) \in \left\{ \Delta U^{FEM}(t, \boldsymbol{\theta}), \Delta V^{FEM}(t, \boldsymbol{\theta}), F^{FEM}(t, \boldsymbol{\theta}) \right\} \tag{8}$$

and where the amplitude of a signal $f(t)$ is denoted by $[f(t)]_T$:

$$[f(t)]_T = \max_{t \in [0,T]} f(t) - \min_{t \in [0,T]} f(t) \tag{9}$$

The residual error $E^Q(t)$ is presented in figures 12d, 13d and 14d. For all loading conditions, the residual error is between -5% and +5% for ΔU and F. For the 75° loading condition, the residual error is between -5% and +5% for ΔV as well. This range of 10% shows that the proposed direct model and the minimization procedure are able to reproduce measurements rather satisfyingly. However, the amplitude of ΔV is much lower than ΔU for the 45° and 15° loading conditions. Thus, the relative measurement uncertainty $\zeta^{\Delta V}$ is much larger than $\zeta^{\Delta U}$ as detailed in table 9. As a consequence, the residual error $E^{\Delta V}(t)$ is very large (between -40% and 70% for the 45° loading condition and between -15% and 15% for the 15° loading condition). This measurement uncertainty issue does not compromise the inverse method, since the weight on ΔV is not significant for the minimization of φ (for the 45° and 15° loading conditions).

The residual error $E^Q(t)$ quantifies the ability of the direct model to approximate the experimental tests, but the identification itself is responsible for uncertainties independently on the residual error $E^Q(t)$ (i.e., even though computed signals $Q(t, \boldsymbol{\theta}^I)$ were in perfect agreement with experimental data $Q(t)$). Thus, the identified computed signal $Q(t, \boldsymbol{\theta}^I)$ is taken as a reference in order to overcome the bias between measurements and computations. The *sensitivity* of the direct model is introduced as follows:

$$S^Q(t, \boldsymbol{\theta}) = \frac{Q(t, \boldsymbol{\theta}) - Q(t, \boldsymbol{\theta}^I)}{\left[Q(t, \boldsymbol{\theta}^I) \right]_T} \tag{10}$$

Because of the relative measurement uncertainty ζ^Q, all material parameters $\boldsymbol{\theta}$ such as $S^Q(t, \boldsymbol{\theta}) \leq \zeta^Q$ is acceptable. Thus, the uncertainty is estimated by computing the range of acceptable variations of material parameters from the identified vector $\boldsymbol{\theta}^I = \left(\theta_1^I, \cdots, \theta_N^I \right)$. For each identified parameter θ_j^I (where $1 \leq j \leq N$ with $N = 8$) considered independently, one can obtain an

upper bound of the uncertainty. Indeed, consider $\Delta \boldsymbol{\theta}_j^n = (0, \cdots, \Delta \theta_j^n, \cdots, 0)$ where $\Delta \theta_j^n$ is a $n\%$ variation on θ_j^I and:

$$S_j^{Q,n}(t) = S^Q(t, \boldsymbol{\theta}^I + \Delta \boldsymbol{\theta}_j^n) \tag{11}$$

If $\left| S_j^{Q,n}(t) \right| > \zeta^Q$, then, $\boldsymbol{\theta}^I + \Delta \boldsymbol{\theta}_j^n$ is not acceptable and $n\%$ is an upper bound of the uncertainty for θ_j^I. This estimation is presented in principle in figure 17.
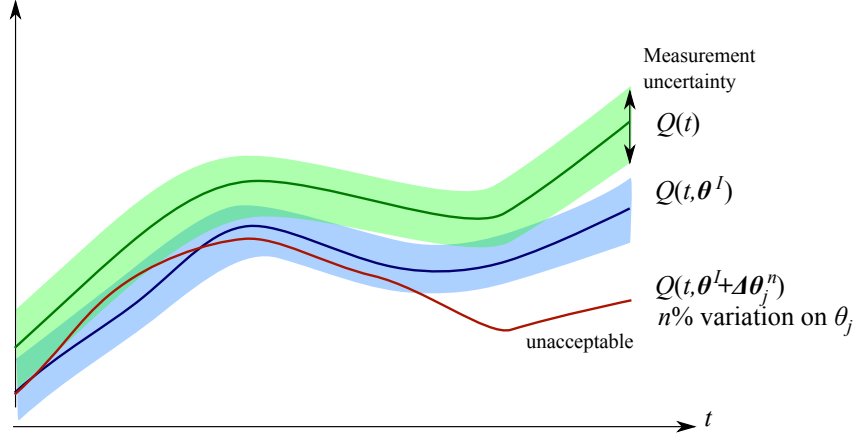

Figure 17: Uncertainty estimation : comparison of a measured signal and two different computed signals

Furthermore, a covariance-like matrix related to the sensitivity $S_j^{Q,n}(t)$ is introduced in order to give a synthetic tool. Consider:

$$s_j^{Q,n}(t) = S_j^{Q,n}(t) - \left\langle S_j^{Q,n}(t) \right\rangle_T \tag{12}$$

where, for a signal $f(t)$:

$$\langle f(t) \rangle_T = \frac{1}{T} \int_0^T f(t)\mathrm{d}t \tag{13}$$

The covariance-like matrix is defined as follows:

$$M_{jl}^Q = \left\langle s_j^{Q,n}(t) s_l^{Q,n}(t) \right\rangle_T \tag{14}$$

On the one hand, diagonal terms (variance) enable to evaluate an overall sensitivity of the direct model for each material parameter. On the other hand, non-diagonal terms (covariance) enable to estimate if variations of two different material parameters have similar effect, that can make the identification difficult. The qualitative interpretation of the covariance-like matrix is as follows. If diagonal terms $\left| M_{jj}^Q \right|$ are higher than the measurement uncertainty variance, then the corresponding parameter may be identified within $n\%$ (with $n = 5$ in this paper). The measurement uncertainty variance is obtained for ΔU and ΔV (and for each loading condition) by analyzing the estimation of measurement noise $\delta^{DIC}(t)$ presented in figure 16. Indeed, $\delta^{DIC}(t)$ is divided by the considered signal amplitude and the variance denoted by Var^Q (where Q should be replaced by ΔU or ΔV) is computed and listed in table 10. Considering the poor estimation of measurement uncertainties, it should be reminded that only the order of magnitude is meaningful.

In addition, the smaller non-diagonal terms $\left| M_{jl}^Q \right|$ are in comparison to $\sqrt{M_{jj}^Q M_{ll}^Q}$ and the easier it is to distinguish the effect of the two corresponding material parameters variations.

23

Similar qualitative reasoning also holds for the variance of measurement uncertainty Var^Q in comparison to $\sqrt{M_{jj}^Q M_{ll}^Q}$. Thus, a qualitative interpretation of non-diagonal terms is to consider that the effect of the variation of the two corresponding parameters can be distinguished if the following criterion is verified:

$$C_{jl}^Q = \frac{\left|M_{jl}^Q\right| Var^Q}{M_{jj}^Q M_{ll}^Q} \ll 1 \tag{15}$$

Table 10: Estimation of the variance of measurement uncertainties for $\Delta U, \Delta V$ for the three different loading conditions

Condition	$Var^{\Delta U}$ ($\times 10^{-5}$)	$Var^{\Delta V}$ ($\times 10^{-5}$)
45°	1	1628
15°	23	1188
75°	4	9

The sensitivity $S_j^{Q,n}(t)$ is presented in figures 18a, 19a, 20a and 20c for $n = 5\%$ for different material parameters variations. The corresponding covariance matrices are presented in figures 18b, 19b, 20b and 20d. Only the most interesting components are presented (i.e., components that exceed significantly measurement uncertainties). The sensitivity corresponding to the global signal F is below 3% for all loading conditions, showing the necessity of having local contributions ΔU and ΔV that are more sensitive to the joint material parameters. For all loading conditions, two criteria are used to determine if a material parameter can be identified within 5%. The sensitivity $S_j^{Q,n}(t)$ should exceed the measurement uncertainty threshold ζ^Q on the one hand, and the corresponding diagonal term M_{jj}^Q of the covariance matrix should also exceed the variance of measurement uncertainties Var^Q. Results are presented in table 11 where the symbol + indicates that only one criterion is verified, ++ indicates that both criteria are verified and - indicates that none is verified. Elastic parameters E_J and ν_J (Young's modulus and Poisson ratio) cannot be identified within 5% on the basis of the 45° and the 15° loading conditions. However, since the adhesive joint is assumed to be isotropic, ν_J can be obtained from the 75° loading condition and fixed for the other loading conditions. The value of the Young's modulus E_J identified from the 75° loading condition is slightly adapted for the other loading conditions on the basis of the first frames of the DIC at the beginning of the test (where the other material parameters have very few influence). Unlike elastic parameters, plastic parameters $\sigma_J^0, \sigma_J^1, \sigma_J^2$ should be discussed for each loading condition individually, because each condition is related to a specific tensorial stress state corresponding to a specific point on the yield surface. Thus, the points of the yield surface are not identified with the same uncertainty.

Results presented in table 11 are not sufficient to conclude that material parameters labeled ++ or + in table 11 can be identified within 5%. Indeed, non-diagonal terms of the covariance matrices should also be analyzed with respect to the criterion proposed in (15) in order to determine if one can distinguish the effects of variations of two parameters. Thus, matrices $C_{jl}^{\Delta U}$ introduced in (15) are computed for parameters labeled ++ or + in table 11 and are presented for all loading conditions in figure 21. For the 45° loading condition, all material parameters verify the criterion (15) with a maximum $C_{jl}^{\Delta U} = 0.16$ that is fairly smaller than 1. For the 15° loading condition, most material parameters verify the criterion (15) excepted ε_J^1 and σ_J^0

$(C_{jl}^{\Delta U} = 0.25)$ whose effects may be slightly difficult to distinguish with respect to the variance of measurement uncertainties. However, for the 75° loading condition, $E_J, \sigma_A^0, \sigma_A^1$ and P_1 cannot be identified within 5% because they have very similar effects ($C_{jl}^{\Delta U} > 0.5$) that is also visible in figure 20a. This work shows this type of uncertainties analysis is of great interest in the identification of material parameters using an inverse method. It gives good insights on the confidence of each identified parameter, and not a single value. A larger experimental database would be useful to determine uncertainties quantitatively.

Table 11: Identification within 5% of the material parameters (the symbol + indicates that only one criterion is verified, ++ indicates that both criteria are verified and - indicates that none is verified.)

	45°	15°	75°
E_J	-	-	+
ν_J	-	-	+
σ_J^0	++	++	++
σ_J^1	++	++	−
$\epsilon_J^1 / \sigma_A^0$	+	+	++
σ_J^2 / σ_A^1	++	-	+
c_1	-	-	-
P_1	++	++	+
P_2	+	-	-

(a) Sensitivity ΔU (b) Covariance matrix $\boldsymbol{M}^{\Delta U}$

Figure 18: Sensitivity and covariance matrix for a 5% variation of $\boldsymbol{\theta}^I$ for the 45° loading condition
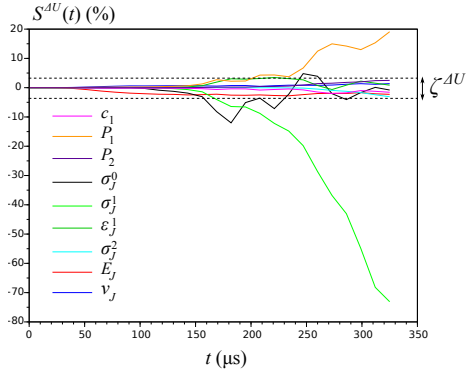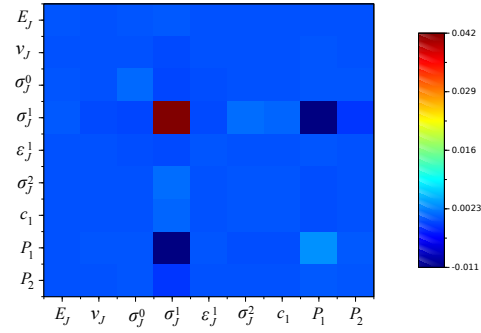
(a) Sensitivity ΔU

(b) Covariance matrix $\boldsymbol{M}^{\Delta U}$

Figure 19: Sensitivity and covariance matrix for a 5% variation of $\boldsymbol{\theta}^I$ for the 15° loading condition
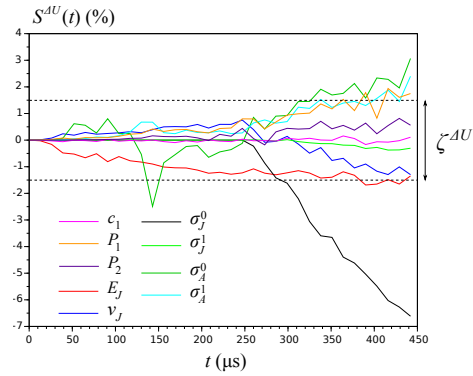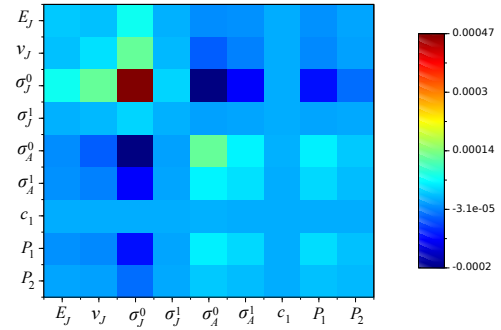
(a) Sensitivity ΔU

(b) Covariance matrix $\boldsymbol{M}^{\Delta U}$
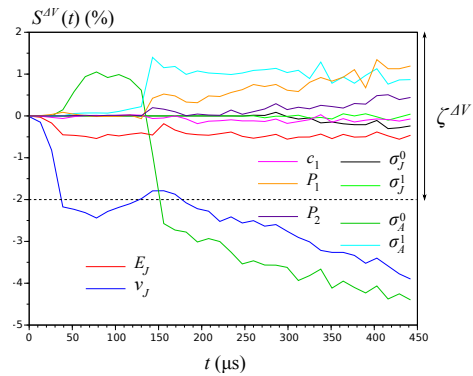
(c) Sensitivity ΔV
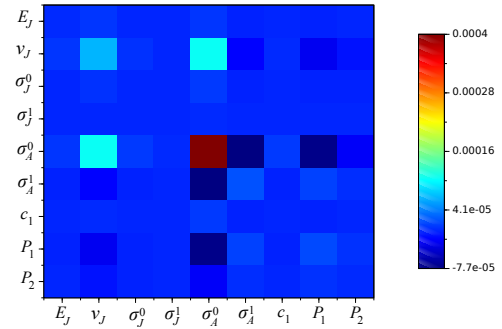
(d) Covariance matrix $\boldsymbol{M}^{\Delta V}$

Figure 20: Sensitivity and covariance matrix for a 5% variation of $\boldsymbol{\theta}^I$ for the 75° loading condition

(a) $C^{\Delta U}$ for the 45° loading condition

(b) $C^{\Delta U}$ for the 15° loading condition

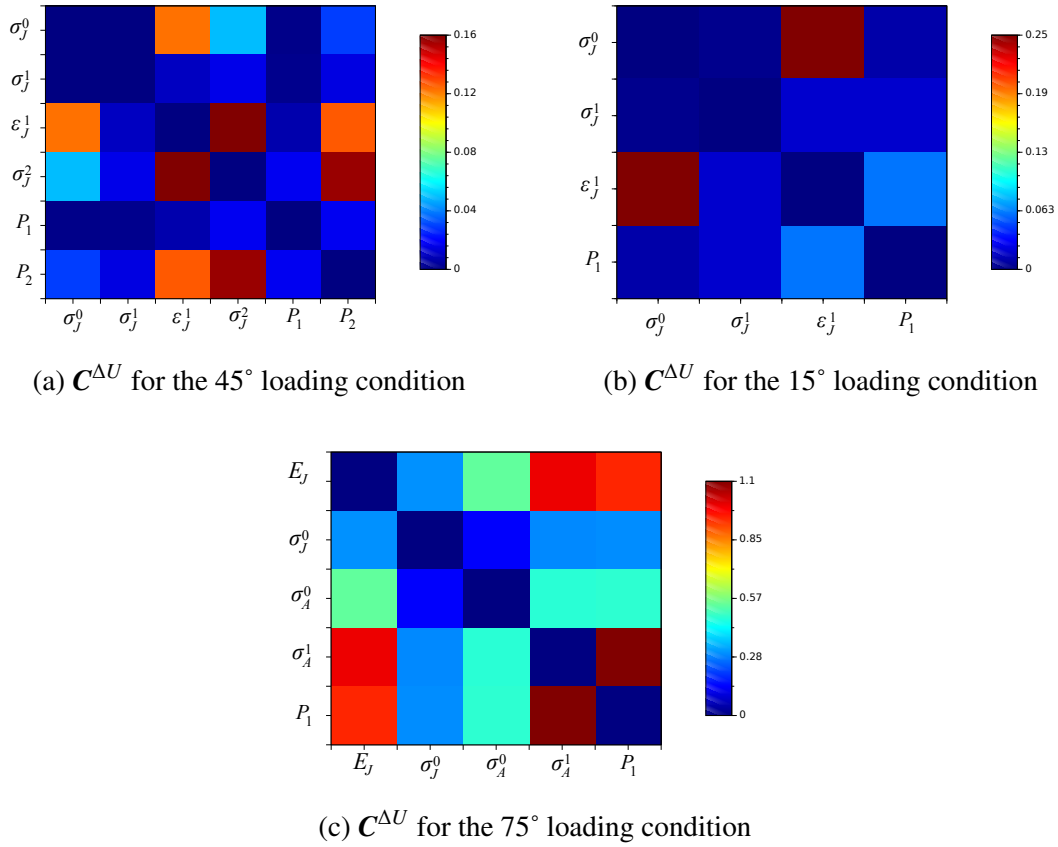(c) $C^{\Delta U}$ for the 75° loading condition

Figure 21: Criterion on non-diagonal terms of the covariance matrix for the three different loading conditions

7. Conclusion

This paper presented a numerical inverse identification method of the material parameters of adhesive joints under multiaxial and dynamic loading conditions. The experimental setup consists of a Split Hopkinson Pressure Bar system with strain rates roughly set to 1000 s^{-1}, a dedicated specimen and local optical measurements processed by Digital Image Correlation. The proposed identification approach, the Finite Element Model Updating method (FEMU) consists in developing a reasonably accurate and fast direct Finite Element simulation of the experiments combined with a Nelder-Mead gradient free minimization of the cost function.

The study proved that a direct FE method mixing 3D and 1D elements for the modeling of the input and output bars provides precise prediction of the time evolution of the mechanical fields and is therefore a good compromise between computation time and accuracy.

The identification procedure combined with an adequate strategy of identifying in several steps: (i) first elastic and then (ii) plastic and finally (iii) failure parameters provided a robust estimation of the material characteristics of adhesive joints. Moreover, the identified parameters were consistent with common knowledge from databases in literature.

The proposed uncertainty analysis provided error estimates of the identified parameters and showed that this information can be obtained with a small additional cost added to the identification method. However, the discussion about uncertainties is purely qualitative but

gives some interesting insights on the confidence one can expect from the identified material parameters.

The results proved that the identification analysis is feasible in a reasonable computational time, but needs at several steps human input to choose the pertinent identification strategy, complexifying the system on a step by step basis. This is because the different model parameters combining finite element meshing choices, with contact model and material behavior are complex and coupled between each other. It is clear that a precise quantative estimation of parameters and their uncertainties would demand a larger experimental data base.

Acknowledgment

References

[1] Jean-Yves Cognard, Romain Créac'hcadec, Laurent Sohier, and Peter Davies. Analysis of the nonlinear behavior of adhesives in bonded assemblies-comparison of tast and arcan tests. *International Journal of Adhesion and Adhesives*, 28(8):393–404, 2008.

[2] Nicolas Carrere, Claudiu Badulescu, Jean-Yves Cognard, and Dominique Leguillon. 3d models of specimens with a scarf joint to test the adhesive and cohesive multi-axial behavior of adhesives. *International Journal of Adhesion and Adhesives*, 62:154–164, 2015.

[3] Gent, A. N. Adhesion of viscoelastic materials to rigid substrates. II. Tensile strength of adhesive joints. *Journal of Polymer Science Part A2: Polymer Physics*, 9(2), 283-294, 1971.

[4] Adams, R. D., Harris, J. A. The influence of local geometry on the strength of adhesive joints. *International Journal of Adhesion and Adhesives*, 7(2), 69-80, 1987.

[5] Mangapatnam Adamvalli and Venkitanarayanan Parameswaran. Dynamic strength of adhesive single lap joints at high temperature. *International Journal of Adhesion and Adhesives*, 28(6):321–327, 2008.

[6] Georges Challita and Ramzi Othman. Finite-element analysis of shpb tests on double-lap adhesive joints. *International Journal of Adhesion and Adhesives*, 30(4):236–244, 2010.

[7] Georges Challita, Ramzi Othman, Pascal Casari, and Khaled Khalil. Experimental investigation of the shear dynamic behavior of double-lap adhesively bonded joints on a wide range of strain rates. *International Journal of Adhesion and Adhesives*, 31(3):146–153, 2011.

[8] Jean-Louis Halary and Françoise Lauprêtre. *Mécanique des matériaux polymères*. Belin, 2015.

[9] Hamed Abdi, J Papadopoulos, H Nayeb-Hashemi, and A Vaziri. Enhanced elastic-foundation analysis of balanced single lap adhesive joints. *International Journal of Adhesion and Adhesives*, 72:80–91, 2017.

[10] Richard Villey, Pierre-Philippe Cortet, Costantino Creton, and Matteo Ciccotti. In-situ measurement of the large strain response of the fibrillar debonding region during the steady peeling of pressure sensitive adhesives. *International Journal of Fracture*, 204(2):175–190, 2017.

[11] Julien Chopin, Richard Villey, David Yarusso, Etienne Barthel, Costantino Creton, and Matteo Ciccotti. Nonlinear viscoelastic modeling of adhesive failure for polyacrylate pressure-sensitive adhesives. *Macromolecules*, 51(21):8605–8610, 2018.

[12] Hassanipour M, chsner A. Implementation of a pressure sensitive yield criterion for adhesives into a commercial finite element code. *J Adhes*, 87(12):112547, 2011.

[13] François Hild and Stéphane Roux. Digital image correlation: from displacement measurement to identification of elastic properties–a review. *Strain*, 42(2):69–80, 2006.

[14] Stéphane Roux and François Hild. Stress intensity factor measurements from digital image correlation: post-processing and integrated approaches. *International journal of fracture*, 140(1):141–157, 2006.

[15] A Gilat, TE Schmidt, and AL Walker. Full field strain measurement in compression and tensile split hopkinson bar experiments. *Experimental Mechanics*, 49(2):291–302, 2009.

[16] H Koerber, J Xavier, and PP Camanho. High strain rate characterisation of unidirectional carbon-epoxy im7-8552 in transverse compression and in-plane shear using digital image correlation. *Mechanics of Materials*, 42(11):1004–1019, 2010.

[17] C C Roth, G Gary, and D Mohr. Compact SHPB System for Intermediate and High Strain Rate Plasticity and Fracture Testing of Sheet Metal. *Experimental mechanics*, 55:1803–1811, 2015.

[18] JD Seidt, VT Kuokkala, JL Smith, and A Gilat. Synchronous full-field strain and temperature measurement in tensile tests at low, intermediate and high strain rates. *Experimental Mechanics*, 2(57):219–229, 2016.

[19] A Janin, A Constantinescu, D Weisz-Patrault, R Neviere, M Stackler, and W Albouy. A new multiaxial specimen for determining dynamic properties of adhesive joints. *Experimental Mechanics*, 2018. (in press).

[20] Laurent Rota. *Application de méthodes inverses au dépouillement de l'essai aux barres de Hopkinson.* PhD thesis, Ecole Polytechnique X, 1997.

[21] Rolf Mahnken and Erwin Stein. Parameter identification for viscoplastic models based on analytical derivatives of a least-squares functional and stability investigations. *International Journal of Plasticity*, 12(4):451–479, 1996.

[22] A Gavrus, Elisabeth Massoni, and JL Chenot. An inverse analysis using a finite element model for identification of rheological parameters. *Journal of Materials Processing Technology*, 60(1-4):447–454, 1996.

[23] Andrei Constantinescu and Nicolas Tardieu. On the identification of elastoviscoplastic constitutive laws from indentation tests. *Inverse Problems in Engineering*, 9(1):19–44, 2001.

[24] Romain Forestier, Yvan Chastel, and Elisabeth Massoni. 3d inverse analysis model using semi-analytical differentiation for mechanical parameter estimation. *Inverse Problems in Engineering*, 11(3):255–271, 2003.

[25] Andrei Constantinescu and Ky Dang Van. A global computational approach in engineering problems: identification and fatigue. *Lecture Notes-AMAS*, 2004.

[26] Huy Duong Bui. *Inverse problems in the mechanics of materials*. Editions of the University of Karadanga, 1997.

[27] Victor Isakov. *Inverse problems for partial differential equations*, volume 127 of *Applied mathematical sciences*. Springer, 1998.

[28] Albert Tarantola. *Inverse problem theory and methods for model parameter estimation*, volume 89. siam, 2005.

[29] Stéphane Avril, Marc Bonnet, Anne-Sophie Bretelle, Michel Grediac, François Hild, Patrick Ienny, Félix Latourte, Didier Lemosse, Stéphane Pagano, Emmanuel Pagnacco, et al. Overview of identification methods of mechanical parameters based on full-field measurements. *Experimental Mechanics*, 48(4):381, 2008.

[30] Marc Bonnet and Andrei Constantinescu. Inverse problems in elasticity. *Inverse problems*, 21(2):R1, 2005.

[31] A Janin, A Constantinescu, D Weisz-Patrault, R Neviere, M Stackler, and W Albouy. An experimental technique for the characterization of adhesive joints under dynamic multiaxial loadings. *Procedia Engineering*, 197:52–59, 2017.

[32] G Gary. David instruction manual, 2005.

[33] Alexandre Jouan and Andrei Constantinescu. A critical comparison of shear tests for adhesive joints. *International Journal of Adhesion and Adhesives*, 84:63 – 79, 2018.

[34] Han Zhao and Gérard Gary. On the use of shpb techniques to determine the dynamic behavior of materials in the range of small strains. *International Journal of Solids and structures*, 33(23):3363–3375, 1996.

[35] Han Zhao and Gérard Gary. A new method for the separation of waves. application to the shpb technique for an unlimited duration of measurement. *Journal of the Mechanics and Physics of Solids*, 45(7):1185–1202, 1997.

[36] Kamal Safa and Gérard Gary. Displacement correction for punching at a dynamically loaded bar end. *International Journal of Impact Engineering*, 37(4):371–384, 2010.

[37] Shiming Dong, Yang Wang, and Yuanming Xia. A finite element analysis for using brazilian disk in split hopkinson pressure bar to investigate dynamic fracture behavior of brittle polymer materials. *Polymer testing*, 25(7):943–952, 2006.

[38] QZ Wang, F Feng, M Ni, and XP Gou. Measurement of mode i and mode ii rock dynamic fracture toughness with cracked straight through flattened brazilian disc impacted by split hopkinson pressure bar. *Engineering Fracture Mechanics*, 78(12):2455–2469, 2011.

[39] Christian C Roth and Dirk Mohr. Effect of strain rate on ductile fracture initiation in advanced high strength steel sheets: experiments and modeling. *International Journal of Plasticity*, 56:19–44, 2014.

[40] Users Manual Abaqus. Abaqus, 2006.

[41] WRD Wilson and S Sheu. Real area of contact and boundary friction in metal forming. *International journal of mechanical sciences*, 30(7):475–489, 1988.

[42] MPF Sutcliffe. Surface asperity deformation in metal forming processes. *International Journal of Mechanical Sciences*, 30(11):847–868, 1988.

[43] Shen Sheu and William RD Wilson. Mixed lubrication of strip rolling. *Tribology transactions*, 37(3):483–493, 1994.

[44] Python Python 2.7, 2011.

[45] J Kennedy and R Eberhart. Particle swarm optimization (pso). In *Proc. IEEE International Conference on Neural Networks, Perth, Australia*, pages 1942–1948, 1995.

[46] Guannan Wang, Wenqiong Tu, and Marek-Jerzy Pindera. Tailoring the moduli of composites using hollow reinforcement. *Composite Structures*, 160:838–853, 2017.